



## Journal of Advanced Research in Fluid Mechanics and Thermal Sciences

Journal homepage:  
[https://semarakilmu.com.my/journals/index.php/fluid\\_mechanics\\_thermal\\_sciences/index](https://semarakilmu.com.my/journals/index.php/fluid_mechanics_thermal_sciences/index)  
ISSN: 2289-7879



# CFD Simulation of Laminar Rotating Flow Inside a Membrane Filter Vessel

Soufyane Ladeg<sup>1,2,\*</sup>, Nadji Moulai-Mostefa<sup>2</sup>, Luhui Ding<sup>3</sup>

<sup>1</sup> Faculty of Sciences and Technology, University of Tissemsilt, Rue de Bougara-Ben Hamouda, 38004, Tissemsilt, Algeria

<sup>2</sup> Materials and Environmental Laboratory, University of Medea, Ain D'Heb, 2001 Medea, Algeria

<sup>3</sup> EA 4297 TIMR, Technological University of Compiègne, 60205 Compiègne Cedex, France

### ARTICLE INFO

#### Article history:

Received 20 September 2022

Received in revised form 16 January 2023

Accepted 22 January 2023

Available online 12 February 2023

#### Keywords:

Wall shear stress; rotating flow;  
membrane; dead-end filtration; CFD

### ABSTRACT

In this study, computational fluid dynamics (CFD) was used to simulate a steady-state rotating flow inside a filtration system. The shape of a 3-D vessel was designed and then meshed using ANSYS design modular (DM) and workbench mesh. The laminar viscous regime was employed; it was identified using the Reynolds number formula. As a boundary layer, the zero inlet velocity and atmospheric pressure were imposed on the inlet boundary. The obtained results showed that for a rotating velocity of 50 rpm, the shear stress distribution on the membrane surface is extremely low, except for four narrow regions situated between the extremities of the impeller and the vessel wall. The pressure variation versus z axes, below the impeller, was almost constant, and it was unevenly distributed on the membrane surface, with two areas of negative pressure. The velocity values below the impeller were higher than those above. This study provides good insights that suggest designing the impeller shape under the most extreme conditions (rotating velocity, flow regime, and pressure inlet) of the membrane. The filtration process will be performed in a future study.

## 1. Introduction

Tangential filtration by membranes is a technique widely used in a variety of industries [1,2]. It was employed in product concentration (agri-food, pharmaceuticals), and in separation and elimination of industrial liquid effluents [3]. In addition, dead-end filtration was historically used in laboratory and medical filtration. In contrast to conventional cross-flow membrane processes, the feed is fed vertically to the membrane element; it passes through the membrane with concentrated solids, laying down a thick layer of cake on the membrane's surface. The benefits of dead-end filtration include high product recovery, least expensive and easiest to implement [4,5]. So, many systems were proposed for separation by frontal filtration such as dialysis, coffee filters, and sand filtration. Among these systems, the Amicon cell has been employed in the extraction of inulin from chicory juice, ultrafiltration of sugar beet juice and apple juice clarification [6-8]. If we classify this last process as tangential or frontal filtration, the filtration by the Amicon cell has a significant

\* Corresponding author.

E-mail address: [ladeg.soufyane@yahoo.fr](mailto:ladeg.soufyane@yahoo.fr)

<https://doi.org/10.37934/arfmts.103.1.201210>

disadvantage, which manifests itself as rapid membrane clogging despite the use of dynamic filtration.

Clogging is the most significant impediment to the filtration process. In any case, an increase in shear stress improves the permeate flow and, as a result, a decrease in particle accumulation on the membrane's surface [9,10]. In the case of the Amicon cell, the clogging particles are eroded by the high shear stress using a stirrer. Several studies were devoted to modeling and forecasting of clogging and permeate flux. Among the techniques used, computational fluid dynamics (CFD) as a modeling and/or process simulation software was widely utilized in many engineering membrane filtration systems [11,12].

CFD plays a significant role in engineering predictions that it is now regarded as a new 3D dimension in fluid dynamics, alongside pure experiment and pure theory as the 2D other dimensions [13–15]. Moreover, the fluid flow prediction using modern CFD software can unveil many features of dynamic flow, heat and mass transfer, chemical reactions, and many other related physico-chemical phenomena by solving a set of complicated mathematical equations [16,17]. Recently, CFD was used by Ladeg *et al.*, [18] in order to model the thickness of the cake layer produced by clogging on the membrane surface; it was found that in the case of tangential filtration, the cake layer thickness is highly dependent on pressure and shear stress values. To assess the hydrodynamic efficiency, reactor shape configuration, and impeller design, Ding *et al.*, [16] used CFD to simulate a gas-liquid flow inside a stirred-tank reactor in the laboratory scale. They found that the biohydrogen production was more efficient with different impeller types and speeds. To understand the liquid-phase mixing process in stirred slurry reactors at various stages of solid suspension, a CFD model was developed by Kasat *et al.*, [19]. The two-fluid flow model was used in a stirred reactor, whereas the multiple reference frames (MRF) model was utilized to simulate the impeller rotation.

By using CFD, we will be able to reveal the distribution of the shear stress, the pressure on the membrane surface, the circumferential velocity behavior, and the impeller's shape usefulness, respectively. The goal of this study was to conduct a preliminary study on the usefulness of CFD using ANSYS Fluent on single-phase flow (water) inside a filtration vessel (Amicon cell). The CFD model was validated by its comparison with the theoretical model. This will therefore lead to another future study using turbulent regime, and different types of fluids and impellers.

## 2. Material and Methods

### 2.1 Theoretical Background

Navier-Stokes equations (NSE) outline every aspect of everything that is flowing across the cosmos; they describe the Newtonian fluid movement [13,20,21]. However, finding exact solutions to the NSE poses insurmountable mathematical challenges because there are non-linear partial differential equations (PDE). However, they often make possible, with a rough resolution, to denote a solution which has a simple explicit form. An exact solution is sometimes simplified to the solution of ordinary differential equations [20,22].

In the case of a laminar regime ( $Re < 10^5$ ), the simplified NSE that describe the Newtonian fluid flow in cylindrical coordinates are given by [23]

$$\rho \left( u_r \frac{\partial u_r}{\partial r} - \frac{u_\theta^2}{r} + u_z \frac{\partial u_r}{\partial z} \right) = -\frac{\partial p}{\partial r} + \mu \left( \frac{\partial^2 u_r}{\partial r^2} + \frac{1}{r} \frac{\partial u_r}{\partial r} + \frac{\partial^2 u_r}{\partial z^2} \right) \quad (1)$$

$$\rho \left( u_r \frac{\partial u_\theta}{\partial r} + \frac{u_r u_\theta}{r} + u_z \frac{\partial u_\theta}{\partial z} \right) = \mu \left( \frac{\partial^2 u_\theta}{\partial r^2} + \frac{1}{r} \frac{\partial u_\theta}{\partial r} + \frac{\partial^2 u_\theta}{\partial z^2} \right) \quad (2)$$

$$\rho \left( u_r \frac{\partial u_z}{\partial r} + u_z \frac{\partial u_z}{\partial z} \right) = -\frac{\partial p}{\partial z} + \mu \left( \frac{\partial^2 u_z}{\partial r^2} + \frac{1}{r} \frac{\partial u_z}{\partial r} + \frac{\partial^2 u_z}{\partial z^2} \right) \quad (3)$$

According to the simplified NSE described above, some simplifications can be made [22]. Consequently, the simplified NSE reduce to:

Consequently, the following simplified equations result (Eq. (5) and Eq. (6))

$$\rho \frac{u_\theta^2}{r} = \frac{\partial p}{\partial r} \quad (4)$$

$$\frac{\partial^2 u_\theta}{\partial r^2} + \frac{1}{r} \frac{\partial u_\theta}{\partial r} = 0 \quad (5)$$

Eq. (5) can also be written as follows

$$u_\theta'' + \frac{1}{r} u_\theta' = 0 \quad (6)$$

Where  $u_\theta$  denotes the circumferential velocity.

This equation admits two particular solutions:  $u_{1\theta} = 1/r$  and  $u_{2\theta} = r$ . The general solution is a combination of the two solutions, with the following boundary conditions: (i) at the extremity ( $r=R_1$ ) of the impeller,  $u_\theta = R_1 \cdot \omega$ , (ii) in the extremity of the vessel wall ( $r=R_2$ ),  $u_\theta = 0$ .

By replacing  $u_\theta$  with its expression, we can determine the constants  $c_1$  and  $c_2$

$$\omega R_1 = c_1 R_1 + \frac{c_2}{R_1} \quad (7)$$

$$0 = c_1 R_2 + \frac{c_2}{R_2} \quad (8)$$

As a result, we found

$$c_1 = -\frac{\omega R_1^2}{R_2^2 - R_1^2} \quad (9)$$

$$c_2 = \frac{\omega R_1^2 R_2^2}{R_2^2 - R_1^2} \quad (10)$$

Finally, the final expression of the circumferential velocity versus radius is expressed by Eq. (12)

$$u_{\theta}(r) = \frac{1}{R_2^2 - R_1^2} \left[ \omega \frac{(R_1^2 R_2^2)}{r} - r(\omega_1 R_1^2) \right] \quad (11)$$

The only purpose of this relation (Eq. (11)) is to make a comparison in the thin boundary between the impeller extremity and the vessel's wall.

The Reynolds formula was used to establish the flow regime for each value of the rotating speed ( $\Omega$ ) [24].

$$Re = \frac{\omega d^2 \rho}{\mu} = \frac{\Omega \pi d^2 \rho}{30 \mu} \quad (12)$$

where  $\omega$  is the angular velocity ( $\omega = \Omega 2\pi / 60$ ),  $d$  is the impeller diameter,  $\rho$  and  $\mu$  are respectively the density and the dynamic viscosity of the liquid.

## 2.2 Material

The set-up of the dead-end ultrafiltration is presented in Figure 1. The ultrafiltration was performed in a stirred cell Amicon with an effective membrane surface ranged between 28.7 and 31.7 cm<sup>2</sup>, with a maximum volume of 180 mL [4,7].

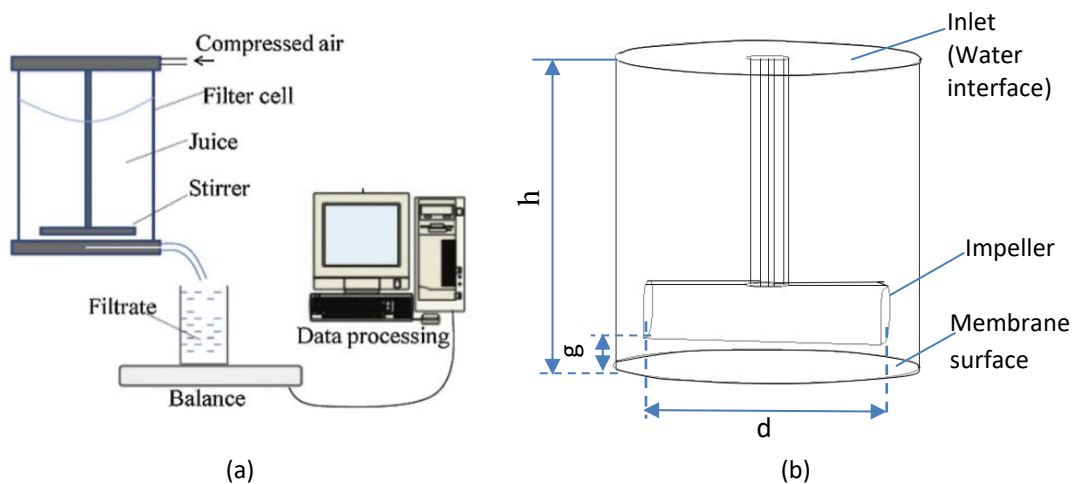


**Fig. 1.** (a) Experimental model dead-end filtration; (b) Filtration cell designed by CFD

The CFD model is cylinder-shaped and has an 80 mm diameter and 115 mm height ( $h$ ). The membrane and the impeller are separated by a 5 mm ( $g$ ), and the impeller has a cylindrical form with a diameter of 5 mm and a length of 60 mm ( $d$ ).

## 2.3 Methods of Investigation and Grid

In this investigation, CFD was used to study the stress distribution, the pressure and the circumferential velocity profiles as a function of radius on the surface of the membrane. Indeed, Ansys fluent was employed, by means of which the ultrafiltration cells were designed, and then the

mesh was created to discretize the domains into tiny control volumes. Therefore, the numerical method might approach the conservation equations. For around  $4.10^5$  cells, the grid independence is nearly achieved [25,26]. This grid configuration was used in the subsequent CFD simulation. For this, an organized tetrahedral mesh with 516593 elements and 95432 nodes was selected. A tiny mesh was utilized to improve the computation stability and accuracy [27]. The number of elements was increased by using refinement near the membrane and the cell walls of the impeller. A broad perspective of the generated mesh is depicted in Figure 2. A water-liquid as cell zone material was chosen, with a density of  $998 \text{ kg/m}^3$  and dynamic viscosity of  $0.001 \text{ kg/m.s}$ . In terms of boundary conditions, a pressure of 1 bar and zero velocity on the inlet were imposed. The entire computational domain and the movement of the impeller in the cell zone were referred to a single rotating reference frame (SRF). The impeller and the cell zone have the same absolute rotating flow; the wall was maintained at zero relative rotating velocity with no slip. Depending on the rotating speed flow, a viscous laminar regime was used at 50 rpm.

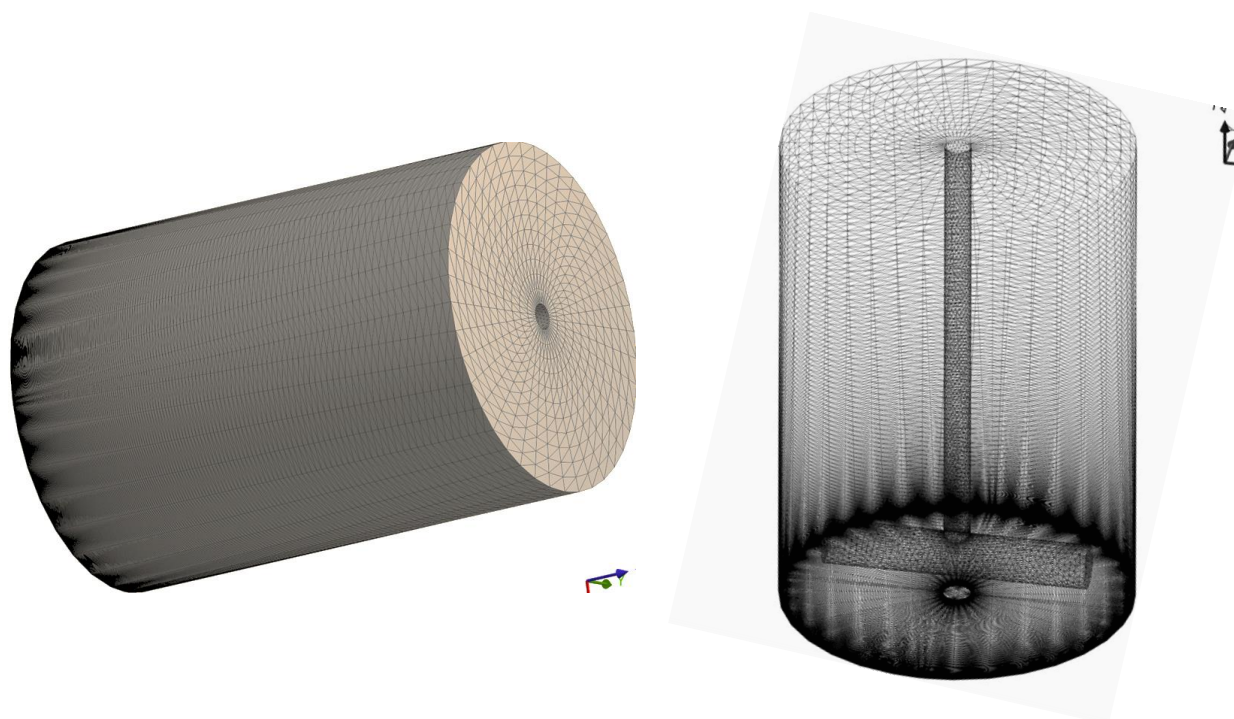
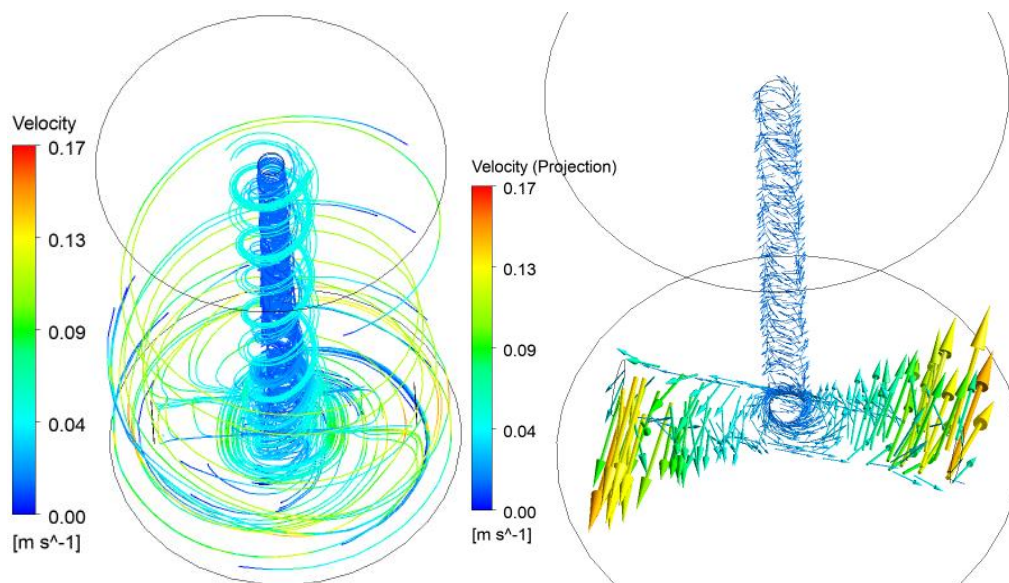


Fig. 2. The meshed cell

### 3. Results and Discussion

Figure 3 represents the velocity streamlines for a rotating velocity of 50 rpm. We noted that the impeller pushed the fluid toward the walls of the cell where it splashed back. It was then guided vertically in a cyclone spiral flow in opposite directions towards the inlet of the tank, thus creating a uniform flow near the impeller. After that, there is an axial jet of liquid emerging from the side of the tank. It was also observed that the velocity streamlines have spread out uniformly to other parts of the cell. This kind of impeller will not effectively disperse the particles during mixing to produce a more homogeneous solution. According to Akiti *et al.*, [28], an impeller with a straightforward blade as an anchor produces less turbulent flow, which results in less mixing of inhomogeneous liquid. The velocity projection increases progressively from the center until the extremity of the impeller. Figure 4 shows clearly the variation of the circumferential velocity versus the radius of cell filtration for 50 rpm and in three different regions inside the cell vessel. We noted that for the region above the

velocity increased rapidly in radius between 0 and 0.02 m, and then in radius between 0.02 and 0.03 m the velocity remains constant with a little decrease. However, below and through the impeller the velocity magnitude has two behaviors. First, the circumferential velocity increases gradually with the radius ranged between 0 and 0.03 m, and then decreases rapidly to a zero value in the extremity of the vessel. The first behaviour may be explained by the example of flow between rotor stator disc, where the velocity is proportional to the disc radius ( $v_{\theta} = r.\omega$ ) [20]. The behaviour of the velocity magnitude after the extremity of the impeller (exactly for a radius value of 0.03 m) was observed in the flow between two coaxial cylinders when the inner cylinder rotated with an angular velocity and the outer cylinder remained stable.



**Fig. 3.** Streamline and vector projection velocity at a rotating velocity of 50 rpm

The values deduced from Eq. (11) are represented by the square symbol in the range of radius values between the end of the wheel and the wall of the tank (0.03-0.04). The behavior of the curve throughout this range is consistent with the results predicted by CFD. It should be emphasized that the flow model between two coaxial cylinders is at the origin of the theoretical model. It can be deduced that in the case of the CFD model, the velocity drops between the two ends (the impeller and the vessel wall) is deep.

The pressure variation as a function of radius is depicted in Figure 5. As shown in Figure 5(b), the pressure gradually increases until it reaches a value of 0.5 Pa in the radius region between 0 and 0.015 m. It then gradually decreases to 0.1 Pa at 0.03 m (a radius value greater than 0.015), which is the impeller's extremity. After a radius of 0.03 m, the pressure rapidly increases, reaching a maximum of 2.8 Pa at the cell vessel's extremity. Figure 5(a) depicts the pressure distribution as a horizontal circular plane, with the high pressure area in front of the membrane in red, and the low pressure area in green. Under the two-impeller extremities, there are two blue zones with negative pressures. The inversion of the pressure vector in this region may help to explain the greatest wall shear stress in this zone.

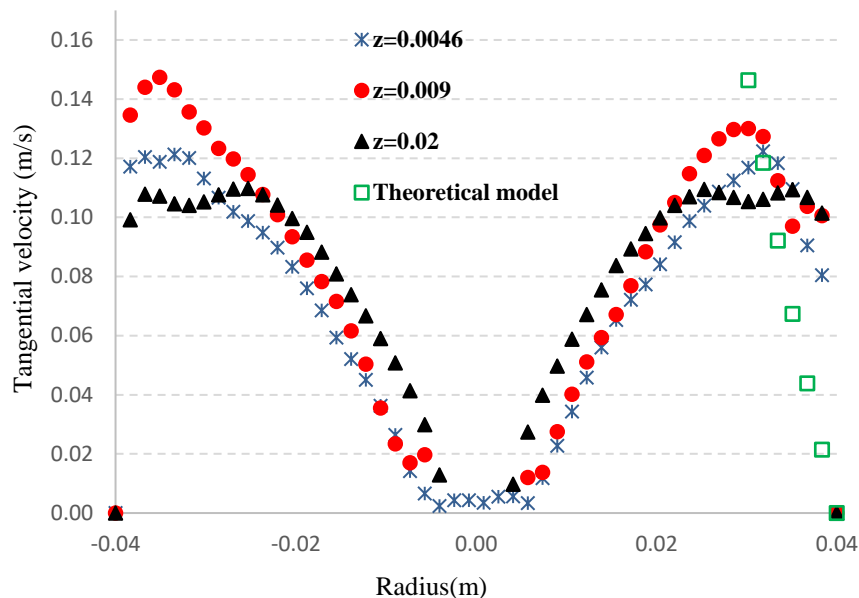


**Fig. 4.** Velocity profile variation versus  $r$  and  $z$  axes at a rotating velocity of 50 rpm

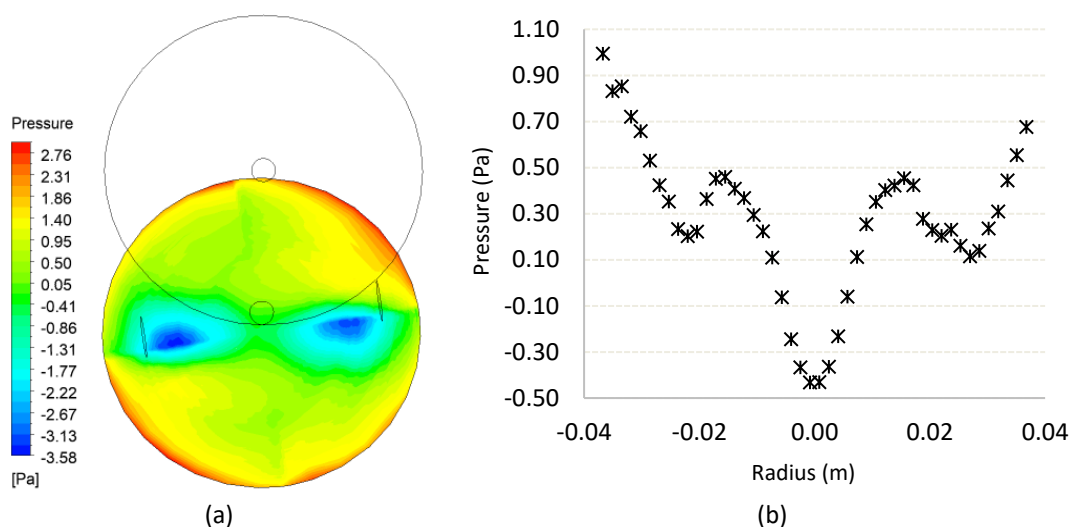


**Fig. 5.** Pressure variation versus radius at rotating velocity of 50 rpm; on the membrane surface ( $z=0$ )

The scatter plot in Figure 6 shows the variation of the pressure at four different levels in the  $z$ -axis coordinates. At  $z = 0$ , it is the cloud of points representing the variation of the pressure as a function of the radius at the surface of the membrane. However, for values of  $z = 0.0046, 0.009,$  and  $0.025$  the pressure corresponds to the position below, across and above the impeller, respectively. Moreover, the pressure variation through and up the impeller is almost the same except for the pressure distribution on the membrane surface, where the pressure decreases more than in any other scatter plot, and especially in the extremity of the impeller. However, the pressure distribution above the impeller (at  $z = 0.025$  m) is very low in comparison with the values obtained on the surface of the membrane.

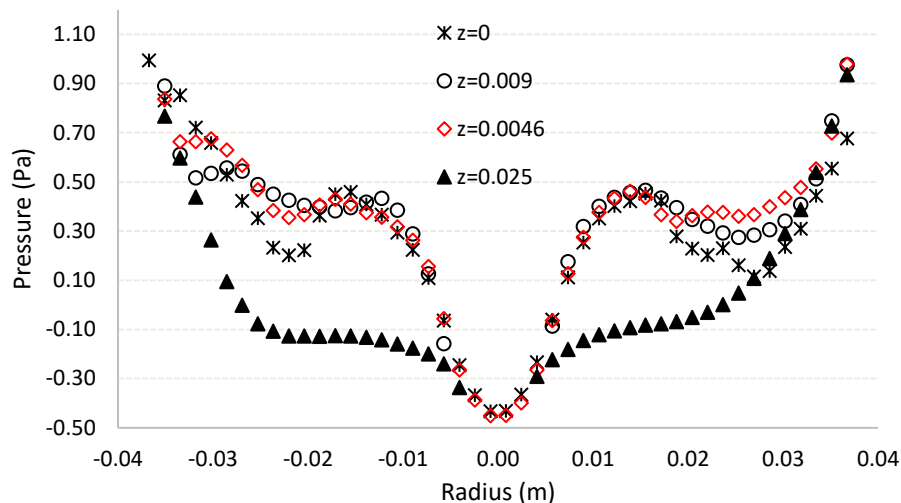


Fig. 6. Pressure variation versus  $r$  and  $z$  axes at a rotating velocity of 50 rpm

Figure 7 represents the distribution and variation of the shear stress according to the radius of the membrane. First, we noted that the shape of the stress variation is parabolic in the radius zone between 0 and 0.03 m where the impeller exists (Figure 7(b)). Up to a value of 0.03 m, the shear stress decreases rapidly until a value of 0 Pa at the level of the membrane edge. The maximum value obtained (1.15 Pa) is located in four regions as shown in Figure 7(a). It must be mentioned that the shear stress is a good tool to evacuate the accumulation of the particles deposited on the surface of the membrane. Consequently, the shear stress results showed how the impeller geometry could generate low or high shear stress values.

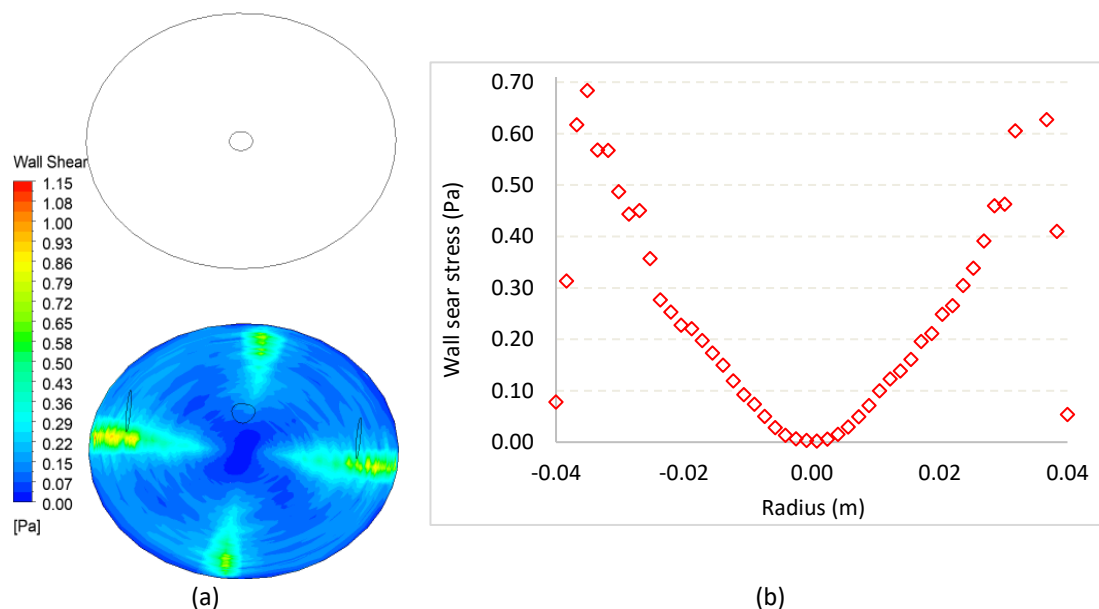


Fig. 7. Wall shear stress variation versus radius at rotating velocity of 50 rpm

#### 4. Conclusion

The performed numerical study revealed the variation in the distribution of pressure and stress on the membrane's surface, highlighting areas of low and high values of shear stress. The pressure variation along the  $z$ -axis was found nearly constant due to the small gap between the impeller and the membrane surface. The theoretical model of the circumferential velocity inspired by the two

coaxial cylinders correctly describes the CFD model only in the gap between the tip of the impeller and the cell walls. During the simulation, we left the gap between the impeller and the membrane unchanged ( $g$  is constant), but we found that as we moved away from the membrane, the pressure fell along  $Z$ . The industrial model (*Amicon 8200*) maintains the gap between the impeller and the membrane at  $g=5$  mm. In addition, the results obtained made it possible to predict another design by modifying the geometry of the impeller by comparing with other shapes (rectangular, triangular...), and its examination under different operating conditions of filtration (pressure and rotating velocity) in order to identify the best conditions to improve the permeate flow.

### Acknowledgements

This work was supported by the Laboratory of Materials and Environment (LME, University of Medea, Algeria).

### References

- [1] Madsen, Emil, Johann Kaiser, Ulrich Krühne, and Manuel Pinelo. "Single pass tangential flow filtration: Critical operational variables, fouling, and main current applications." *Separation and Purification Technology* 291 (2022): 120949. <https://doi.org/10.1016/j.seppur.2022.120949>
- [2] Zhang, Wenxiang, Nabil Grimi, Michel Y. Jaffrin, and Luhui Ding. "Leaf protein concentration of alfalfa juice by membrane technology." *Journal of Membrane Science* 489 (2015): 183-193. <https://doi.org/10.1016/j.memsci.2015.03.092>
- [3] Galambos, Ildikó, Jesus Mora Molina, Péter Járay, Gyula Vatai, and Erika Bekássy-Molnár. "High organic content industrial wastewater treatment by membrane filtration." *Desalination* 162 (2004): 117-120. [https://doi.org/10.1016/S0011-9164\(04\)00034-7](https://doi.org/10.1016/S0011-9164(04)00034-7)
- [4] Singh, Rajindar. *Membrane technology and engineering for water purification: application, systems design and operation*. Butterworth-Heinemann, 2014.
- [5] Staszak, Katarzyna, Karolina Wieszczycka, and Bartosz Tylkowski, eds. *Membrane Technologies: From Academia to Industry*. Walter de Gruyter GmbH & Co KG, 2022. <https://doi.org/10.1515/9783110688269>
- [6] Zhu, Zhenzhou, Olivier Bals, Nabil Grimi, Luhui Ding, and Eugene Vorobiev. "Qualitative characteristics and dead-end ultrafiltration of chicory juice obtained from pulsed electric field treated chicories." *Industrial Crops and Products* 46 (2013): 8-14. <https://doi.org/10.1016/j.indcrop.2013.01.014>
- [7] Zhu, Zhenzhou, Houcine Mhemdi, Luhui Ding, Olivier Bals, Michel Y. Jaffrin, Nabil Grimi, and Eugene Vorobiev. "Dead-end dynamic ultrafiltration of juice expressed from electroporated sugar beets." *Food and Bioprocess Technology* 8 (2015): 615-622. <https://doi.org/10.1007/s11947-014-1427-2>
- [8] Fuenmayor, Carlos Alberto, Solomon Mengistu Lemma, Saverio Mannino, Tanja Mimmo, and Matteo Scampicchio. "Filtration of apple juice by nylon nanofibrous membranes." *Journal of Food Engineering* 122 (2014): 110-116. <https://doi.org/10.1016/j.jfoodeng.2013.08.038>
- [9] Belfort, Georges, Robert H. Davis, and Andrew L. Zydney. "The behavior of suspensions and macromolecular solutions in crossflow microfiltration." *Journal of Membrane Science* 96, no. 1-2 (1994): 1-58. [https://doi.org/10.1016/0376-7388\(94\)00119-7](https://doi.org/10.1016/0376-7388(94)00119-7)
- [10] Luo, Jianquan, Zhenzhou Zhu, Luhui Ding, Olivier Bals, Yinhua Wan, Michel Y. Jaffrin, and Eugene Vorobiev. "Flux behavior in clarification of chicory juice by high-shear membrane filtration: evidence for threshold flux." *Journal of Membrane Science* 435 (2013): 120-129. <https://doi.org/10.1016/j.memsci.2013.01.057>
- [11] Ould-Dris, A., M. Y. Jaffrin, D. Si-Hassen, and Y. Neggaz. "Analysis of cake build-up and removal in cross-flow microfiltration of  $\text{CaCO}_3$  suspensions under varying conditions." *Journal of Membrane Science* 175, no. 2 (2000): 267-283. [https://doi.org/10.1016/S0376-7388\(00\)00411-7](https://doi.org/10.1016/S0376-7388(00)00411-7)
- [12] Mondal, Sourav, and Sirshendu De. "A fouling model for steady state crossflow membrane filtration considering sequential intermediate pore blocking and cake formation." *Separation and Purification Technology* 75, no. 2 (2010): 222-228. <https://doi.org/10.1016/j.seppur.2010.07.016>
- [13] Ali, Mohammed Qasim, and Barhm Mohamad. "A review of the design and control using computational fluid dynamics of gasoline direct injection engines." *Diagnostyka* 23 (2022). <https://doi.org/10.29354/diag/153373>
- [14] Kriby, Saliha, Mohamed Announ, and Tayeb Kermezli. "2D CFD simulation to investigate the thermal and hydrodynamic behavior of nanofluid flowing through a pipe in turbulent conditions." *CFD Letters* 11, no. 11 (2019): 58-75.
- [15] Subramaniam, Thineshwaran, and Mohammad Rasidi Rasani. "Pulsatile CFD Numerical Simulation to investigate

- the effect of various degree and position of stenosis on carotid artery hemodynamics." *Journal of Advanced Research in Applied Sciences and Engineering Technology* 26, no. 2 (2022): 29-40. <https://doi.org/10.37934/araset.26.2.2940>
- [16] Ding, Jie, Xu Wang, Xue-Fei Zhou, Nan-Qi Ren, and Wan-Qian Guo. "CFD optimization of continuous stirred-tank (CSTR) reactor for biohydrogen production." *Bioresource Technology* 101, no. 18 (2010): 7005-7013. <https://doi.org/10.1016/j.biortech.2010.03.146>
- [17] Wang, Xu, Jie Ding, Nan-Qi Ren, Bing-Feng Liu, and Wan-Qian Guo. "CFD simulation of an expanded granular sludge bed (EGSB) reactor for biohydrogen production." *International Journal of Hydrogen Energy* 34, no. 24 (2009): 9686-9695. <https://doi.org/10.1016/j.ijhydene.2009.10.027>
- [18] Ladeg, Soufyane, Nadji Moulai-Mostefa, Aissa Ould-Dris, and Luhui Ding. "Modeling of surface fouling on the surface of a rotating disk membrane using CFD and numerical study." *Desalination and Water Treatment* 190 (2020): 52-61. <https://doi.org/10.5004/dwt.2020.25699>
- [19] Kasat, Gopal R., Avinash R. Khopkar, V. V. Ranade, and Aniruddha Bhalchandra Pandit. "CFD simulation of liquid-phase mixing in solid-liquid stirred reactor." *Chemical Engineering Science* 63, no. 15 (2008): 3877-3885. <https://doi.org/10.1016/j.ces.2008.04.018>
- [20] Drazin, Philip G., and Norman Riley. *The Navier-Stokes equations: a classification of flows and exact solutions*. No. 334. Cambridge University Press, 2006. <https://doi.org/10.1017/CBO9780511526459>
- [21] Wah-Yen, Tey, Yutaka Asako, Nor Azwadi Che Sidik, and Goh Rui-Zher. "Governing equations in computational fluid dynamics: Derivations and a recent review." *Progress in Energy and Environment* 1 (2017): 1-19.
- [22] Schlichting, Hermann, and Joseph Kestin. *Boundary layer theory*. Vol. 121. New York: McGraw-Hill, 1961.
- [23] Torras, C., J. Pallares, R. Garcia-Valls, and M. Y. Jaffrin. "Numerical simulation of the flow in a rotating disk filtration module." *Desalination* 235, no. 1-3 (2009): 122-138. <https://doi.org/10.1016/j.desal.2008.02.006>
- [24] Hashimoto, Shunsuke, Hiroyuki Ito, and Yoshiro Inoue. "Experimental study on geometric structure of isolated mixing region in impeller agitated vessel." *Chemical Engineering Science* 64, no. 24 (2009): 5173-5181. <https://doi.org/10.1016/j.ces.2009.08.024>
- [25] Guan, Xiaoping, Xinju Li, Ning Yang, and Mingyan Liu. "CFD simulation of gas-liquid flow in stirred tanks: Effect of drag models." *Chemical Engineering Journal* 386 (2020): 121554. <https://doi.org/10.1016/j.cej.2019.04.134>
- [26] Santos-Moreau, Vania, Lena Brunet-Errard, and Matthieu Rolland. "Numerical CFD simulation of a batch stirred tank reactor with stationary catalytic basket." *Chemical Engineering Journal* 207 (2012): 596-606. <https://doi.org/10.1016/j.cej.2012.07.020>
- [27] Versteeg, Henk Kaarle, and Weeratunge Malalasekera. *An introduction to computational fluid dynamics: the finite volume method*. Pearson Education, 2007.
- [28] Akiti, Otute, Agnes Yeboah, Ge Bai, and Piero M. Armenante. "Hydrodynamic effects on mixing and competitive reactions in laboratory reactors." *Chemical Engineering Science* 60, no. 8-9 (2005): 2341-2354. <https://doi.org/10.1016/j.ces.2004.10.049>